Spatial structures in earthquakes and faults: quantifying similarity in simulated stress fields and natural data sets

Mauro Alberti *

Museo Nazionale dell'Antartide, Sezione di Scienze della Terra, Via Laterina 8, I-53100 Siena, Italy

Abstract

This paper presents an adaptation for fault analysis of the *coherence* method of Kagan and Knopoff [Kagan, Y.Y., Knopoff, L., 1985b. The two-point correlation function of the seismic moment tensor. Geophysical Journal of the Royal Astronomical Society 83, 637–656], understanding *coherence* as a measure of the similarity between fault-slip data for two faults, which can be analytically computed from earthquake or fault moment tensors. Through the use of a customized GIS routine, the degree and distribution of similarity in synthetic and natural fault populations can be calculated as a function of distance between fault/earthquake pairs and their relative orientation. Stress simulations using synthetic data sets reveal that fault populations, which developed under homogeneous stress fields, have a high degree of similarity that increases with the slip tendency of faults. Stress ratio variations, and especially stress axis rotations, lower the coherence values.

Spatial analysis of natural earthquake and fault data sets from the Umbria–Marche region (Northern Apennines, Italy) reveals a common pattern of *coherence* spatial cyclicities in faults/earthquakes controlled by two consecutive tectonic phases, Miocene compression and Plio-Pleistocene extension. The proposed interpretation attributes the spatial cyclicities of Miocene data to syn- to post-faulting folding, in agreement with wavelengths derived from field data. The observed periodicities in earthquakes (1997 Colfiorito–Sellano Umbria–Marche seismic sequence) could, in turn, have been controlled by the Miocene thrust structures, with possible spatial stress field axis rotations and/or stress ratio variations. The spatial characteristics of younger fault/earthquake populations are thus possibly controlled by the characteristics of older tectonic structures, such as fold wavelength or fault spacing.
© 2006 Elsevier Ltd. All rights reserved.

Keywords: Umbria-Marche 1997 seismic sequence; Fault moment tensor; Fault coherence; GIS spatial analysis

1. Introduction

Faults are one of the most widespread and impressive tectonic features of deformed rocks. Unfortunately, their relationships with strain and stress fields are still not completely understood (e.g. Oertel, 1965; Reches, 1978; Twiss et al., 1991, 1993; Pollard et al., 1993; Nieto-Samaniego and Alaniz-Alvarez, 1997). Moreover, stress inversion analysis is based on assumptions, such as the spatial uniformity of the stress field, which may not hold over geological time scales. When considering deformed rock volumes, however, we cannot rule out that original fault characteristics may have been affected by finite deformation. The adopted approach for testing stress uniformity when dealing with data sets covering large regions is to partition the data sets into small sub-regions (usually structural sites) and to check result uniformity *a*

posteriori (e.g. Lavecchia et al., 1994; Gillard and Wyss, 1995). Other approaches consider a probabilistic test of stress field uniformity (e.g. Yin and Ranalli, 1993; Albarello, 2000) or subdivide fault data into homogeneous subsets within a stress space (e.g. Yamaji, 2003; Shan et al., 2003) or a kinematic space (e.g. Nemcok et al., 1999).

A complementary kinematic approach is suggested in this paper: it consists of comparing spatial variations in the similarity of natural data sets to those derived from simulations of synthetic fault populations subjected to uniform and non-uniform stress fields. This approach is inspired by both the scalar quantification of fault orientations proposed by Nemcok et al. (1999) and by geostatistical analysis of scalar 'regionalized' (i.e. geographically continuous) variables in which the squared difference between two separate observations is expressed as a function of distance and/or angle of separation (e.g. Cressie, 1993). Kagan and Knopoff (1985a,b) and Kagan (1992a) used spatial analysis to investigate the similarity between focal solutions of earthquakes. They made use of a *coherence* index that is here applied to fault data.

Since spatial behaviour is the result of strain and stress histories experienced by rock volumes and of the rheologic

* Tel.: +39 5772 33875; fax: +39 5772 33890.
  E-mail address: albertim@unisi.it.

properties of rock volumes, its analysis can highlight kinematic heterogeneities and/or post-faulting deformations. Finite deformation could possibly have an impact on coherence vs. distance relationships and its influence could consequently be inferred from the observed spatial relationships of fault coherence.

Spatial simulations of homogeneous, non-homogeneous and rotated stress fields, possibly resulting from geological situations such as varying stress fields or post-kinematic folding, were performed using tensor notation for fault data processing and an *ad-hoc* customized GIS software. Simulation results are compared with the results from natural fault and earthquake data.

2. Analytical basis

2.1. How can the similarity between two faults be expressed?

If one finds a way to measure the similarity between data from two faults it is then possible to relate this measurement to variations in the distance between faults and in their relative orientation.

At least four methods have been proposed for quantifying the 'similarity' between faults or individual earthquake events. The first two originated in the geophysical community as tools for the analysis of earthquake focal mechanisms, while the other two were proposed in the structural geology community for fault analysis (the latter for calcite twin data also).

The first method is that of Kagan and Knopoff (1985b) and Kagan (1992a). It adopts an analytical approach to calculate the invariants of the fourth-order correlation tensor between two distinct focal mechanisms. The second one, by Kagan (1991, 1992b, 2000), uses quaternions to calculate the four possible rotation axes between two focal mechanisms and selects the solution with the minimum rotation angle as an index of the dissimilarity between two earthquake events.

The third method is presented in Nemcok and Lisle (1995). The value of the similarity index is calculated from: (a) the number of stress tensors that fit both compared faults; (b) the number of stress tensors that fit neither of the compared faults; (c) a user-selected maximum angle of deviation between the observed striation and the theoretical slip vector (as derived from the analysed stress tensor). Pre-processing of the fault data set, required to derive the first two above-mentioned indices, is accomplished through a spherical-grid search performed using a large number of different prescribed stress tensors (Hardcastle and Hills, 1991). The fourth and last method, by Nemcok et al. (1999), is a variant of the previous one. In place of stress tensor compatibility, it uses a right-dihedra compatibility method (Angelier and Mechler, 1977) that allows the separation of heterogeneous fault or calcite twin populations into homogeneous sets. The similarity index calculation uses a dense spherical grid to sample each right-dihedra solution.

This study adopted the first described method, because this tensor approach involves a simple analytical calculation that produces just one unique result (unlike the method of Kagan,

1991 and subsequent) and does not require grid-search pre-processing or the use of spherical grids. Data set analysis yields a series of values derived from all possible matches between one record and all others. As such, these values represent a statistical population that is independent of any preliminary assumptions about stress or strain field characteristics and that can be tested statistically.

2.2. Tensor formulation for fault data

The finite strain tensor D_{ij} for a fault can be derived from the slip vector **u** and the fault normal **v** (Molnar, 1983; Cladouhos and Allmendinger, 1993).

Its components are:

$$D_{ij} = ku_iv_j \quad (i,j = 1, 2, 3) \tag{1}$$

where k is a constant proportional to the fault offset (Molnar, 1983).

Because the magnitude of offset on the fault is rarely determinable in the outcrop, a normalized version of this tensor was adopted:

$$D_{ij}^* = u_iv_j \quad (i,j = 1, 2, 3) \tag{2}$$

This second-rank asymmetric tensor can be decomposed into a symmetric and an anti-symmetric component (Cladouhos and Allmendinger, 1993 and references therein):

$$D_{ij}^* = M_{ij}^* + E_{ij}^* \tag{3}$$

where

$$M_{ij}^* = 0.5\left(D_{ij}^* + D_{ji}^*\right) \tag{4}$$

$$E_{ij}^* = 0.5\left(D_{ij}^* - D_{ji}^*\right) \tag{5}$$

M_{ij}^* represents the incremental pure strain ellipsoid, whose eigenvectors are parallel to T and P kinematic and seismologic axes (Marrett and Allmendinger, 1990), while E_{ij}^* represents an incremental pure rotation. This study restricts strain analysis to the symmetric component of the fault tensor, i.e. to the incremental pure strain orientations expressed by faults. Because M_{ij}^* is symmetric, its value is the same for the two nodal planes (Fig. 1), so that there is loss of information on the rotational component of strain. On the other hand, the method can be applied to both fault and earthquake focal solutions.

The calculation of M_{ij}^* is performed using the formulas given by Aki and Richards (1980), among others (see Appendix A for full details).

2.3. Coherence between fault tensors

Kagan and Knopoff (1985a,b) and Kagan (1992a) proposed to quantify the similarity between seismic tensors using the fourth-rank statistical correlation tensor C_{ijkl} (Eq. 1 in Kagan and Knopoff, 1985b):

$$C_{ijkl}(\mathbf{r}, \tau) = \left\langle M_{ij}(\mathbf{r}_1, t_1)N_{kl}(\mathbf{r}_2, t_2)\right\rangle \tag{6}$$
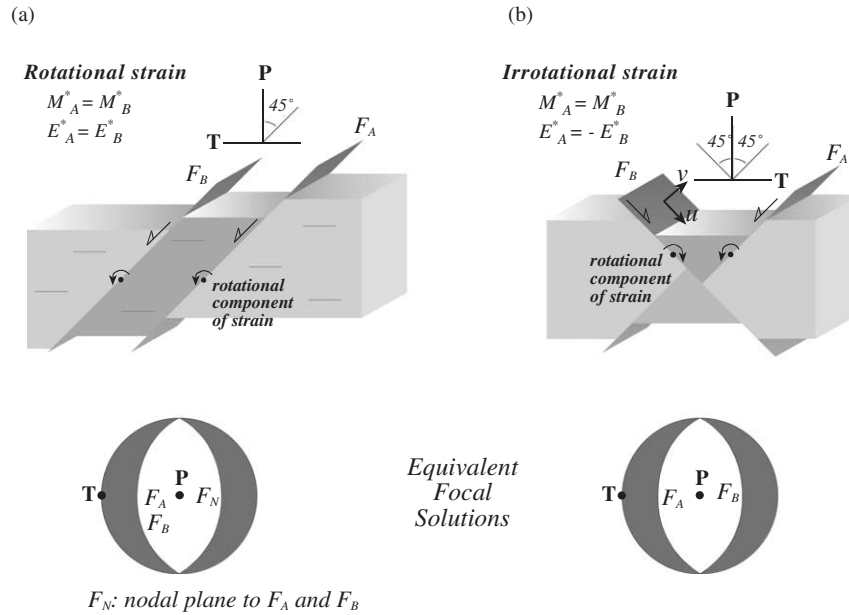
Fig. 1. Two fault configurations giving rise to equivalent symmetric moment tensor components but with opposite anti-symmetric components. In (a) the two faults are parallel and the overall strain is rotational, while in (b) strain is non-rotational, with the second fault parallel to the nodal plane of the first.

where $M(\mathbf{r}_1,t_1)$ and $N(\mathbf{r}_2,t_2)$ are seismic moment tensors separated by a distance $\mathbf{r} = \mathbf{r}_1 - \mathbf{r}_2$ and a time interval $\tau = t_2 - t_1$ and the brackets indicate the average value.

One of the (scalar) invariants of this correlation tensor C_{ijkl} is (Eq. 2 in Kagan and Knopoff, 1985b):

$$J_3 = \langle M_{ij} N_{ij} \rangle \tag{7}$$

Because J_3 is space-independent, it can be used to characterize tensor similarities.

Two equal tensors $M(\mathbf{r}_1,t_1) = N(\mathbf{r}_2,t_2)$ will have:

$$J_3 = -2I_2 \tag{8}$$

where I_2 is one of the invariants of the normalized fault tensor:

$$I_2 = M_{11}M_{22} + M_{11}M_{33} + M_{22}M_{33} - M_{12}^2 - M_{23}^2 - M_{13}^2$$

$$= -0.25 \tag{9}$$

The ratio $J_3/(-I_2)$ can be considered as a dimensionless measure of the coherence of two tensors: it varies between 2 for equal (*coherent* in Kagan and Knopoff terminology) tensors and -2 for *anti-coherent* (i.e. opposite) tensors (Kagan and Knopoff, 1985a,b).

2.4. Calculation of coherence distribution in fault populations

The analysis of coherence distributions in fault populations was performed using an *ad-hoc* ArcView® GIS customization (Alberti, 2005). It allows analysis along user-specified directions and tolerance angles (Fig. 2a–c), in a way similar to directional variogram analyses (e.g. Cressie, 1993). The results can be saved in a summary table or in a detailed text report that can be further queried with database software such as Access®.

3. Theoretical coherence–distance relationships and statistical significance

Spatial variations of coherence may result from many different factors: a non-exhaustive list includes fault-geometry changes (e.g. listric faults), kinematic compatibilities (Marrett and Allmendinger, 1990), dynamic interaction (e.g. Nieto-Samaniego and Alaniz-Alvarez, 1997), spatial and/or temporal stress field variations and post-kinematic deformation (e.g. folding).

This paper investigates the influence of the latter two factors on a synthetic fault data set.

3.1. Synthetic fault data set

A synthetic data set of uniform random faults can be generated using the following formulas of Célérier and Seranne (2001):

$$\text{Strike}: \quad 360° \times R \tag{10}$$

$$\text{Dip angle}: \quad \arccos(R) \tag{11}$$

where R is a random variable uniformly distributed in the [0,1] interval.

The calculation of the dip angle uses $\arccos(R)$ instead of R to avoid generating too many faults with low dip angle, thus resulting in a truly random uniform distribution of fault poles on the hemisphere (Fig. 2b).

To limit the time required for the calculation of simulations with ArcView, the size of the synthetic data set was restricted to 1000 faults, a number that should ensure statistically significant results. In non-directional simulations (e.g. for the homogeneous stress field) the total number of calculated fault couples was almost half a million (499,500), while for
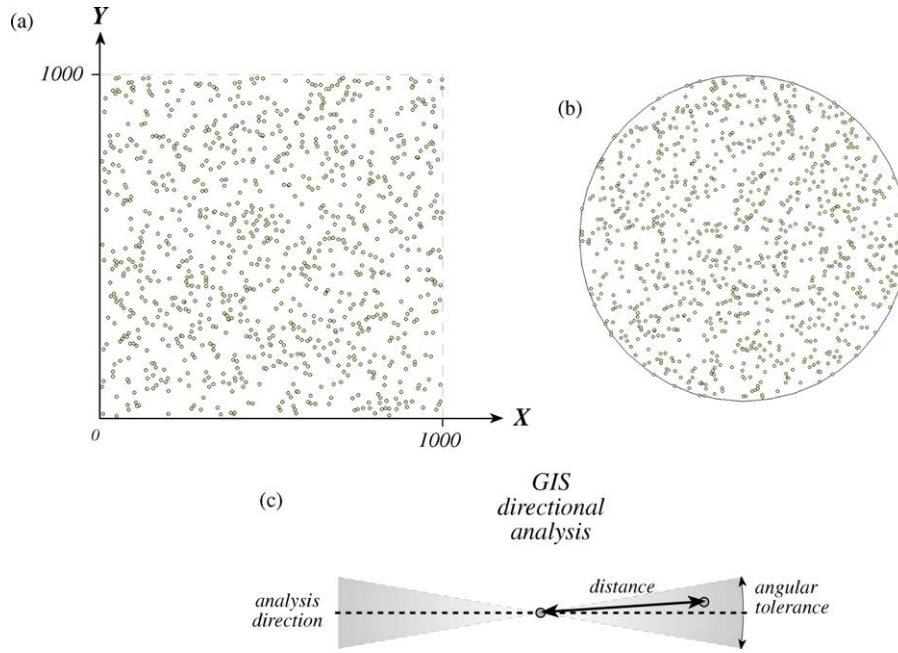
Fig. 2. Synthetic fault data set of 1000 faults with uniform random spatial distribution (a: map representation of fault distribution) and uniform random orientation (b: equal-area, lower-hemisphere stereonet representing poles to fault planes). In the simulations the direction of changing stress ratio and axis orientations is parallel to the x-axis. GIS spatial analyses may be performed along selected directions, with specified angular tolerances and taking into account the distance between analysed fault pairs (c). The stereonet was generated using the ArcView extension by Knox-Robinson and Gardoll (1998).

directional simulations (e.g. the rotating stress field) the number was of the order of some tens of thousands.

A random x–y location within the 0–1000 range was assigned to each fault using ArcView (Fig. 2a).

3.2. Stress simulations

The presented stress simulations are based on the Wallace–Bott theoretical relationships between stress and fault movement (Wallace, 1951; Bott, 1959).

The normal and shear components (σ_N and τ, respectively) of the stress vector σ acting on a plane with normal unit vector n, as a result of a stress tensor T, can be computed through matrix multiplication (Xu, 2004, Eqs. 3 and 4, p. 1318 and references therein):

$$\sigma = T\mathbf{n} \tag{12}$$

$$\sigma_N = \mathbf{n}^t(\sigma\mathbf{n}) \tag{13}$$

$$\tau = \sigma - \sigma_N \tag{14}$$

where n^t is the transpose of n.

It is therefore possible to calculate the *slip tendency* of a fault, i.e. the ratio between the magnitude of τ and σ_N (Morris et al., 1996), which represents one of the main factors regulating the mechanical response of surfaces under a given stress field. Surfaces with a relatively low slip tendency could be expected to act as veins in response to tensile resolved stress or as stylolites in response to compressive stress rather than as slip surfaces. Moreover, small variations in the orientation of the stress field could induce large variations in the shear stress

direction for surfaces with low slip tendency, while surfaces with a high slip tendency are expected to be less influenced by variations in stress field orientation.

A parameter characterizing the shape of a stress tensor is the stress ratio Φ (Orife and Lisle, 2003 and references therein):

$$\Phi = \frac{\sigma_2 - \sigma_3}{\sigma_1 - \sigma_3} \tag{15}$$

whose range is 0 (for $\sigma_2 = \sigma_3$) to 1 (for $\sigma_1 = \sigma_2$).

The simulations with the synthetic data set considered three possible values of the stress ratio Φ: 0.0, 0.5 and 1.0.

A homogeneous stress field, a stress field with fixed axis orientations but changing stress ratio, Φ, and a spatio-temporal rotating stress field (Fig. 3) were simulated. As a final simulation, random slickenline orientations were applied to the synthetic data set.

3.2.1. Homogeneous stress-field

In this simulation the stress field axis orientations were fixed, so that $(\sigma_1 \equiv X) \geqq (\sigma_2 \equiv Y) \geqq (\sigma_3 \equiv Z)$. Results are reported for the complete data set and for fault subsets defined according to the faults with slip tendency greater than the first (25%), second (50%) and third (75%) quartile, respectively.

The derived distributions are all left-skewed (Fig. 4a–c). The full data set and the subset consisting of the three uppermost slip tendency quartiles show no significant change with increasing stress ratio Φ: they all have mean and mode values of around 1.0. The two uppermost quartiles, on the other hand, present a marked difference in distribution between the two Φ end-values (almost identical) and the intermediate Φ value. In the former there are almost no values in anti-coherent and incoherent intervals and the mode at 1.0 presents a sharp
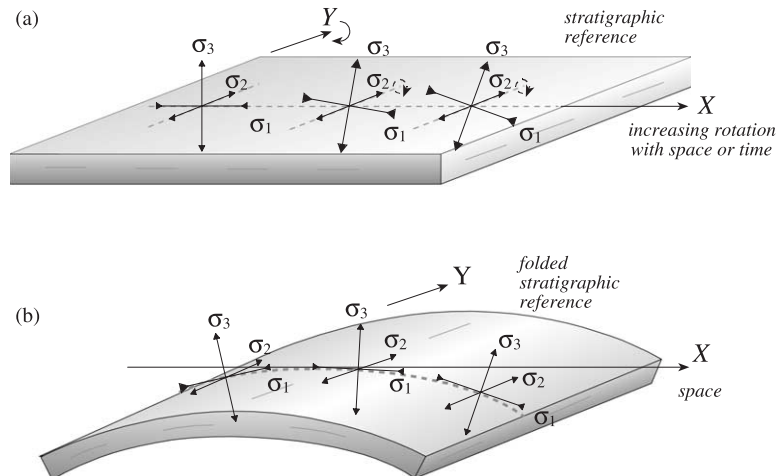
Fig. 3. Illustration of two geological situations with rotating stress field orientations: (a) the stress field rotates along the *x*-direction of a fixed-orientation stratigraphic reference; (b) the stress field orientation is fixed with respect to the stratigraphic reference, and both rotate across the *x*-direction, in response to folding.

increase, accompanied by the development of a new mode at 2.0 coherence; the distributions for $\Phi = 0.5$ show no significant decrease in frequency in the anti-coherent/incoherent intervals, while the mode at 1.0 tends to decrease, with the development of a new mode at 2.0.

According to the results of these simulations, fault populations with high slip tendency and high Φ values should display a high similarity between faults, while those with intermediate Φ values should be dispersed in a large interval, irrespective of the slip tendency of the fault population.

3.2.2. Spatio-temporal variations of Φ with fixed orientations of stress-field axes

This simulation considered a stress field in which the Φ ratio varies spatially from 0 to 1. The results of this analysis are shown in Fig. 5. With increasing Φ ratio variations, the mean value of the coherence decreases in an approximately linear fashion. The mean coherence value ranges from 1.0 to 0.5 for the complete data set and the subset with slip tendency greater than the first quartile value, with a total decrease in the mean coherence of less than 0.5. The subsets with slip tendency greater than the median show a decrease in the mean coherence from 1.0–1.5 to slightly less than 0.5, with a total decrease of 0.5–1.0. The interval of Φ ratio variation without any detectable mean coherence decreases from 0.6 for the complete data set, to 0.1–0.2 for fault subsets with slip tendency greater than the third quartile.

The standard deviation has a constant value of 0.7 for the complete data set, whereas it increases from 0.5 to 0.8 with increasing Φ variations in the uppermost quartile.

3.2.3. Spatio-temporal rotating stress-field/post-kinematic folding of uniform stress field

The simulation of a rotating stress field could be applied to many different geological situations: a space- or time-varying stress field (considering the stress-varying spatial dimension as a temporal one) (Fig. 3a) or post-kinematic folding of rock volumes faulted under a uniform stress field (Fig. 3b).

Assuming an initial stress tensor T, successive matrix multiplications can be used to derive a new value T' in a rotated coordinate system (Kagan and Knopoff, 1985a, p. 433):

$$T' = R(TR^{t}) \tag{16}$$

where R is the rotation matrix and R^{t} is its transpose. R is derived from the orientation of the rotation pole (see Appendix B). The σ_1 and σ_3 stress axes are rotated around a rotation pole parallel to σ_2 (coinciding with the y axis) (Fig. 3). The degree of rotation of the stress field is linearly proportional to the x coordinate; it ranges from $0°$ (for $x=0$) as in the homogeneous stress simulation, to $90°$ (for $x=1000$), corresponding to a complete inversion between σ_1 and σ_3 axes. The sampled fault pairs are located within $\pm 5°$ of the rotation gradient (cf. Fig. 2c).

The results of these analyses are shown in Fig. 6a–c. With increasing total rotations of stress field axes there is an almost linear decrease in mean coherence values from coherent values to incoherent/anti-coherent values. Details vary according to the combined effects of the Φ value and the slip tendency of fault populations.

For $\Phi \approx 0.5$ the slip tendency has limited effects on both the mean coherence and the standard deviation (Fig. 6b). For the two possible Φ end-values, the greater the slip tendency of faults, the greater the initial value of mean coherence (in agreement with the results of the homogeneous stress simulation) and the faster the decrease in mean coherence and the greater the increase in the coherence standard deviation (Fig. 6a and c).

For all slip tendency values, the mean coherence is zero for rotation angles of $45°$ ($\Phi \approx 0.5$) to 55–$60°$ ($\Phi \approx 0.0$ or 1.0).

3.2.4. Random movement simulation

In this simulation a random rake angle ($-180°$ to $180°$) is attributed to the synthetic fault planes. The derived frequency distribution is symmetric around the central value of zero, corresponding to the mean coherence value, with a standard deviation of 0.9 (Fig. 7). The distribution presents a broad, flat
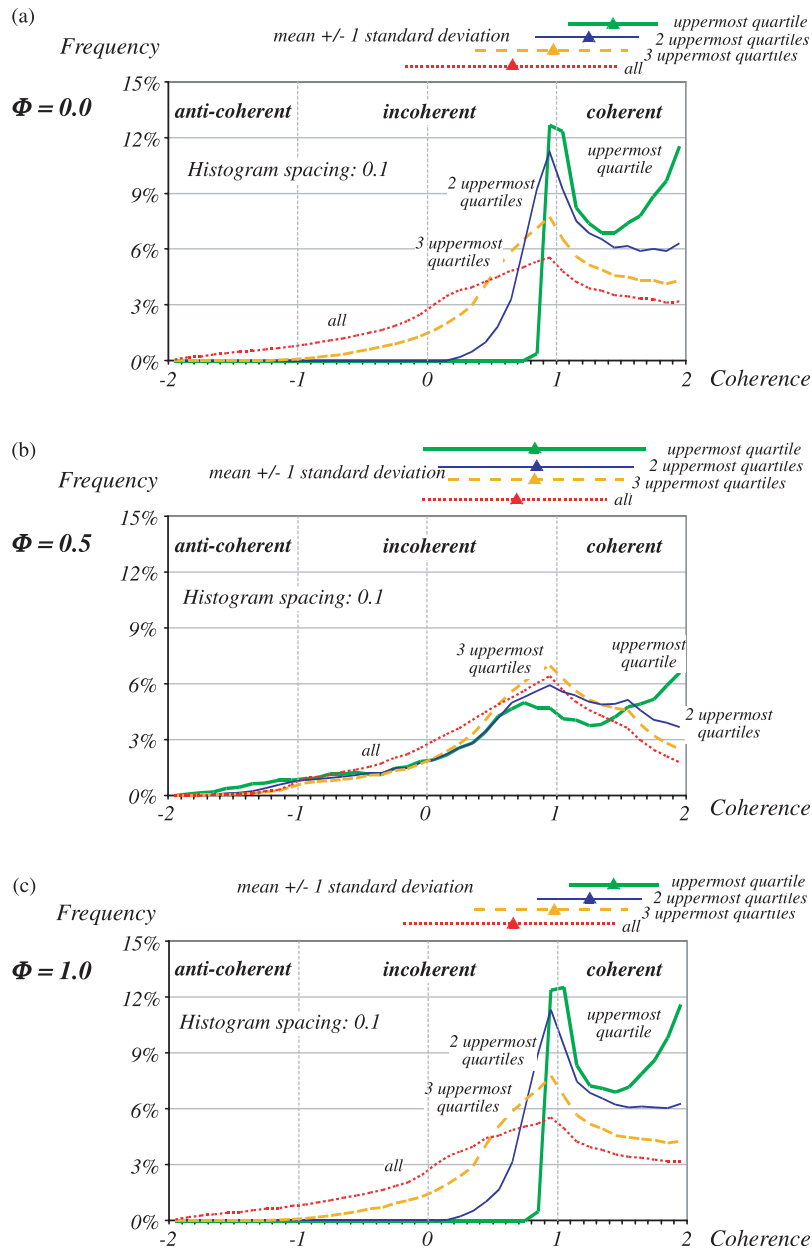
Fig. 4. Coherence frequency distributions for the homogeneous stress simulations: (a) stress ratio $\Phi=0.0$; (b) $\Phi=0.5$; (c) $\Phi=1.0$. The mean coherence value ± 1 standard deviation is plotted above each diagram. The analyses regard the entire synthetic fault data set (*all*), the fault subset with slip tendency greater than the first quartile (corresponding to 75% of the total fault data set, *3 uppermost quartiles*), the fault subset with slip tendency greater than the median (*2 uppermost quartiles*) and the fault subset with slip tendency greater than the third quartile (corresponding to 25% of the total fault data set, *uppermost quartile*). See text for discussion.

plateau in the -1.0 to $+1.0$ interval (incoherent faults pairs) comprising 70% of the total number of fault pairs, and two steep flanks with minima at -2.0 and $+2.0$.

3.3. Sampling and statistical strategies

A sampling scheme for identifying the spatial characteristics of mesofault populations should involve the collection of data in various well-distributed sites, so that coherence values can be calculated for a broad and continuous range of separations. If the possible influence of structures such as pre-existing folds or faults is to be tested, the mean sampling interval should be lower than half the average wavelength

between structures. The establishment of an isotropic and uniform geographic distribution of sampling stations allows directional analyses (cf. Fig. 2c).

The coherence distribution of natural data sets may vary in different separation ranges or different analysis directions. The statistical significance of these variations may be evaluated using statistical tests. The statistical analysis of data sets is generally completed under the assumption that observations were made under identical and independent conditions (Cressie, 1993). For spatially-correlated data, such as fault and earthquake data, rigorous statistical treatment would require the application of declustering techniques prior to statistical testing (e.g. Pardo-Igúzquiza and Dowd, 2004).
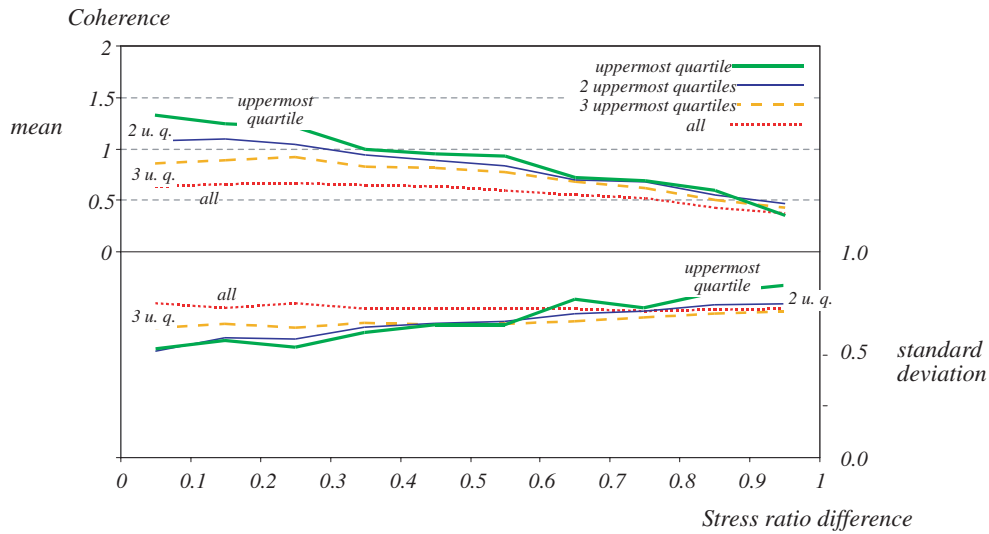
Fig. 5. Results of simulation tests on the influence of Φ stress ratio variations. The upper diagram represents the mean coherence vs. stress ratio difference between fault pairs; the lower diagram represents the corresponding coherence standard deviation. The fault data set subdivision is the same as in Fig. 4. See text for discussion.
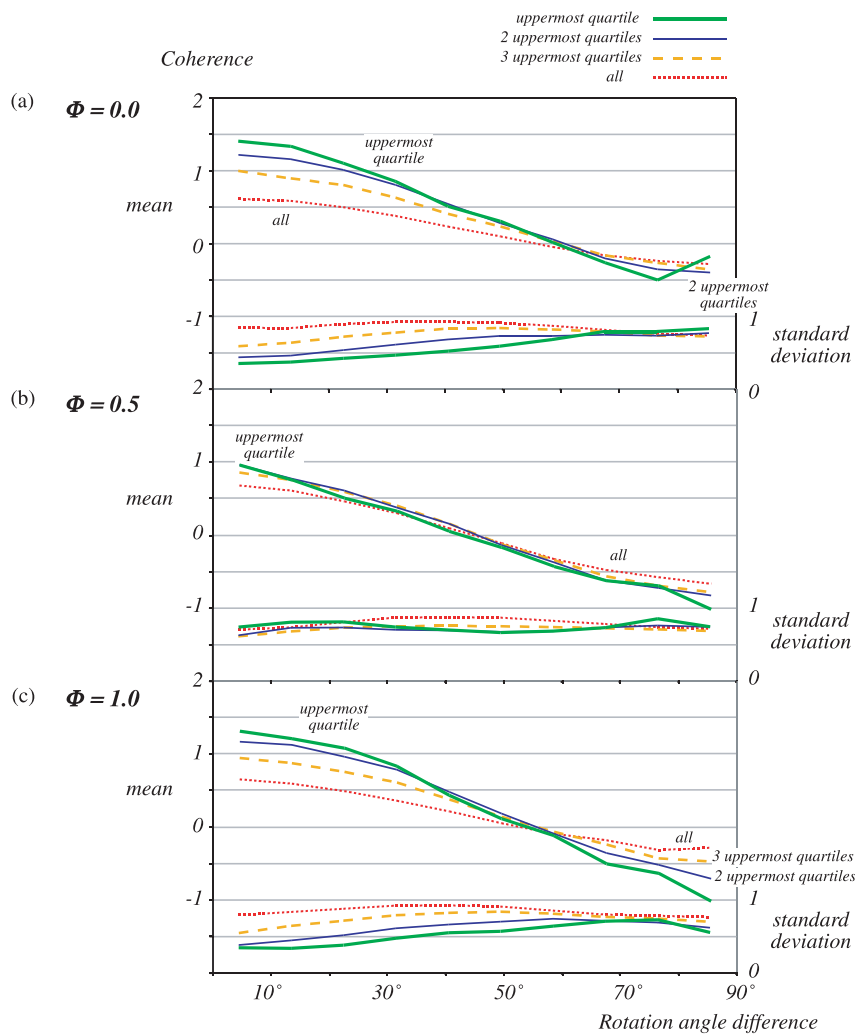

Fig. 6. Results of rotating stress field simulations: (a) stress ratio $\Phi = 0.0$; (b) $\Phi = 0.5$; (c) $\Phi = 1.0$. For each case the upper diagram portion represents the mean coherence vs. relative stress field rotation angle between fault pairs, while the lower portion represents the corresponding coherence standard deviation. The fault data set subdivision is the same as in Fig. 4. See text for discussion.
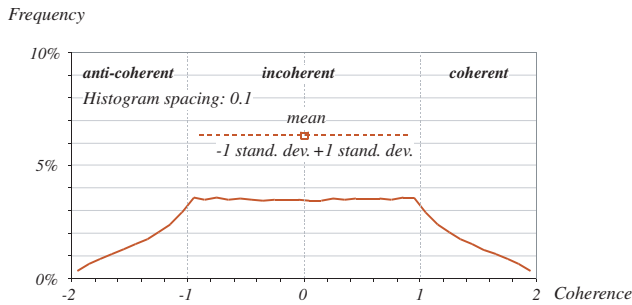
Fig. 7. Frequency distribution of coherence in the random fault data set simulation. See text for discussion.

However, due to the mathematical complexity of such applications, especially when considering tensor data, statistical tests were applied to the raw data; statistical significance should therefore be considered with some caution. Non-parametric tests do not require preliminary assumptions on the distribution type (e.g. Gaussian, log-normal), considering that theoretical coherence distributions display marked variations according to stress field parameters. The classical statistical method to test a hypothesis involves stating a null hypothesis and trying to reject it by deriving a very low probability for it to be true.

Two or more independent data sets derived from analyses in different directions or with different separation intervals may generally be tested. For these sets, the uniformity of the median can be tested using the Kruskal Wallis test (Siegel and Castellan, 1988). If the test rejects the null hypothesis of uniformity, each set may then be compared with the others using the Kolmogorov–Smirnov and the Mann–Whitney tests (Cheeney, 1983). The former is sensitive to the complete

distribution type, while the latter allows the distinction between samples with different medians. When the results of the latter two tests suggest that the two coherence distributions are significantly different, the two fault/earthquake populations may be considered to be different, at least from a kinematic (and possibly a dynamic) point of view.

4. Analysis of natural coherence–distance relationships

4.1. Previous research on the spatial variability of earthquake coherence

The spatial influence on earthquake coherence was investigated by Kagan and Knopoff (1985b) and Kagan (1992a). A compilation of results from these papers is plotted in Fig. 8 (note the logarithmic distance axis). Low-magnitude earthquakes tend to have lower mean coherence values than high-magnitude earthquakes. The monotonic decrease in mean coherence with increasing distance could be interpreted as the result of distance-increasing stochastic disorientation of seismic focal mechanisms (Kagan and Knopoff, 1985b; Kagan, 1992a). In short-range distance intervals of 10^0–10^1 km, typical of structural geology investigations, data from California present a high degree of coherence, with a mean coherence of 1.6–1.4 and a 0.2 decrease over 10 km (Fig. 8). In the 10–100 km interval, evidence of a faster decrease in coherence suggests a change in the mechanisms regulating fault formation. For distances larger than 100 km, fault coherence values fall in the incoherent realm, suggesting a substantial independence of faults.
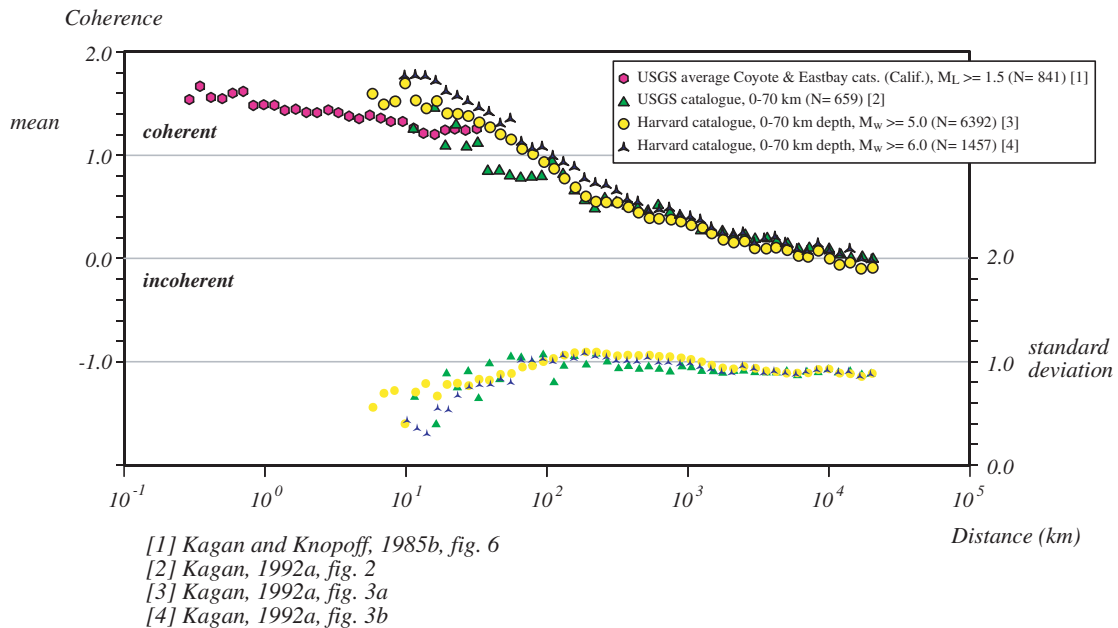
[1] Kagan and Knopoff, 1985b, fig. 6
[2] Kagan, 1992a, fig. 2
[3] Kagan, 1992a, fig. 3a
[4] Kagan, 1992a, fig. 3b

Fig. 8. Logarithmic plot of mean coherence (upper portion) and standard deviation (lower portion) vs. distance for earthquake data deriving from the USGS and Harvard catalogues, from fig. 6 of Kagan and Knopoff (1985b) and from figs. 2 and 3a,b of Kagan (1992a). The mean coherence displays a monotonic decrease with distance, from coherent values for short distances to incoherent values for distances larger than 10^3–10^4 km. Modified after Alberti (in press).

4.2. Earthquakes and faults in a polyphase tectonic settings: the Northern Apennines, Umbria–Marche, Valnerina and Colfiorito–Sellano zones

This study investigated natural examples with a polyphase history from an Umbria–Marche sector of the Northern Apennines (Italy) (Fig. 9). This sector, a deformed pile of thrust sheets, consists of middle Jurassic to Miocene unmetamorphosed marine sediments. Baldanza et al. (1982) and Decandia (1982) identified Jurassic and Cretaceous–Palaeogene synsedimentary extensional tectonics in the Umbria sector. Another extensional deformation phase possibly took place just before the onset of the Miocene contractional orogenic phase (Scisciani et al., 2002). During the upper Miocene, the sedimentary sequence was thrust northeastward, with the development of folds and thrusts, and partial reactivation of Mesozoic–Palaeocene faults as reverse-dextral faults. Some major thrusts were possibly folded (e.g. Scisciani et al., 2002) and palaeomagnetic evidence suggests that thrust sheets were rotated around vertical axes (e.g. Channell, 1992).

From the Late Pliocene onward, a NE–SW extensional deformation phase took place in the Umbria–Marche sector, while a compressive phase is still active in the Adriatic sector, as shown by present-day reverse fault earthquakes (Lavecchia et al., 1994).
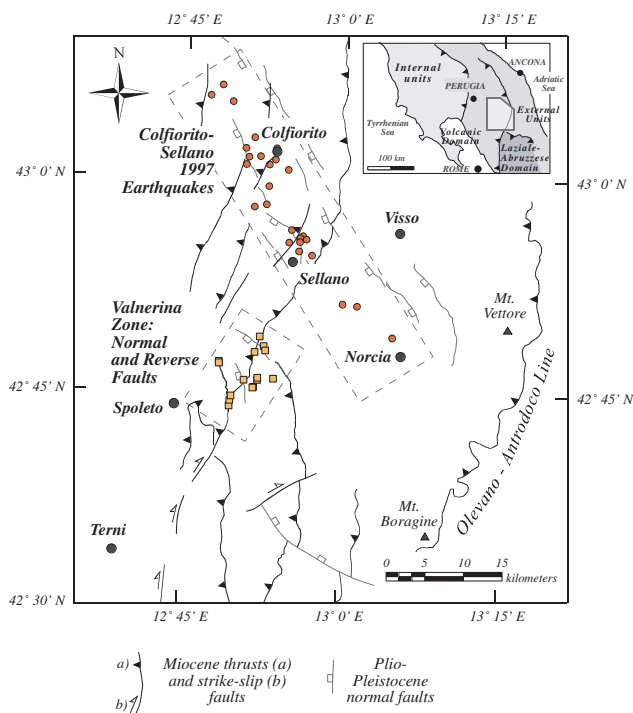

Fig. 9. Structural scheme of the Umbria–Marche region in the Northern Apennines (Italy). The rectangles highlight the two investigated areas: the Colfiorito–Sellano area affected by the 1997 seismic sequence and the nearby Valnerina area with sampled Plio-Pleistocene normal faults and Miocene reverse-dextral faults. Map data are derived mainly from Lavecchia (1985), Boncio and Lavecchia (2000) and Chiaraluce et al. (2005).

Data from the present-day extensional area were used for analysis, including a well-studied normal faulting seismic sequence from 1997–98 (Cattaneo et al., 2000), Plio-Pleistocene normal faults and Miocene reverse-oblique faults from a nearby area, i.e. the Valnerina area between Sellano and Spoleto (Fig. 9).

4.2.1. Coherence–distance relationships in Colfiorito–Sellano 1997 earthquakes

The Colfiorito–Sellano seismic sequence first affected the Umbria–Marche region in September 1997; after some months of quiescence, a second episode occurred in February–April 1998 (Amato et al., 1998; Ekström et al., 1998; Morelli et al., 2000; Chiaraluce et al., 2004; Murru et al., 2004).

Data were recorded by the national seismic network, and by an *ad-hoc* local network installed by ING, Géosciences Azur and Camerino University, immediately after the main seismic events of September 26th 1997 (Amato et al., 1998; Ekström et al., 1998). Additional data were provided by three regional networks and by the temporary stations of the Servizio Sismico Nazionale installed a few days after the main shocks (Cattaneo et al., 2000 and references therein).

The affected area extends for 60 km in a NNW–SSE direction, with fault segments 5–10 km long (Chiaraluce et al., 2004). All the earthquakes originated at shallow depths of 8 km or less, with the exception of two subcrustal earthquakes with focal depths of around 50 km (Cattaneo et al., 2000; Murru et al., 2004). The focal mechanisms and spatio-temporal distribution show mainly normal faulting on two principal shallow, parallel, low-angle (35–45°) faults (Boncio and Lavecchia, 2000; Cattaneo et al., 2000; Murru et al., 2004) with a NE–SW tension axis (Morelli et al., 2000). Subordinate strike-slip and thrust focal mechanisms were also observed (Cattaneo et al., 2000; Chiaraluce et al., 2004, 2005).

The low dip angle of the seismogenic faults is attributed to the reactivation of Late Miocene–Pliocene thrusts (Amato et al., 1998) or to the listric geometry of the normal faults (Boncio and Lavecchia, 2000).

The data set used in this paper comes from Cattaneo et al. (2000). Twenty-six focal mechanisms with M_L magnitudes between 3.7 and 5.9 and depths between 2.0 and 8.7 km were derived from the first P-wave polarities (Table 1 and Fig. 10a–c). The interpreted fault planes dip from NE to S, with mostly normal-oblique motion, and some reverse mechanisms (Fig. 10b). The P–T axis orientations suggest a general SW–NE extension associated with local tendencies to NW–SE compression (Fig. 10c; see also fig. 9 in Cattaneo et al., 2000).

Quantitative relations between coherence and distance are illustrated in Fig. 11a and b (Fig. 11a reports the horizontal 2-D distance, while Fig. 11b also considers the depth component). The Colfiorito–Sellano earthquakes display a spatial cyclicity (Fig. 11a and b): mean coherence values decrease from 1.3–1.4 for very short distances, to a minimum of −0.2 at around 7 km, then tend to increase up to distances of 13.5–14 km, reaching a maximum mean coherence of 1.0, and finally tend to decrease to a secondary minimum of almost 0 at a distance of 21 km. For

Table 1
List of Colfiorito–Sellano 1997 earthquake focal mechanism parameters derived from Table 1 in Cattaneo et al. (2000). Rake is negative for normal movements and positive for reverse movements

Date	Time (UT)	Latitude	Longitude	Depth	Strike (RHR)	Dip	Rake
9/3/1997	22:07	43.0153	12.8795	8.7	170	49	−81
9/26/1997	0:33	43.0207	12.8885	3.8	350	37	−96
9/26/1997	9:40	43.0235	12.8472	6.5	84	61	−138
9/26/1997	9:47	43.1068	12.8032	2.6	18	26	−24
9/26/1997	13:30	43.0095	12.9095	6	60	20	52
9/27/1997	8:08	43.088	12.82	4.2	30	70	−32
9/27/1997	19:56	43.0467	12.8553	4.9	90	61	−124
9/28/1997	11:24	42.969	12.8765	3.5	140	10	76
10/2/1997	10:59	43.0947	12.7843	4.5	330	27	−116
10/3/1997	8:55	43.0342	12.842	5.7	68	51	−91
10/4/1997	6:49	42.925	12.9132	4	94	34	−116
10/4/1997	15:07	42.9307	12.931	2.4	118	23	−120
10/4/1997	16:13	42.9327	12.9357	2.1	102	68	−104
10/4/1997	18:47	42.9287	12.9407	2.1	342	72	−60
10/6/1997	23:24	43.0152	12.843	7	294	58	−122
10/7/1997	5:09	43.0245	12.8652	2.9	122	25	−172
10/12/1997	11:08	42.9107	12.9498	2.2	330	51	−112
10/14/1997	15:23	42.9152	12.9295	4.9	24	62	−100
10/15/1997	22:53	42.9258	12.9303	2	322	50	−56
10/16/1997	4:52	42.9395	12.9173	2	70	62	−168
10/16/1997	12:00	43.0343	12.8905	2	26	63	40
10/19/1997	16:00	42.9658	12.8577	6.5	310	22	−112
10/20/1997	1:27	42.99	12.8795	3.3	358	63	2
10/25/1997	3:08	42.8165	13.0798	2	58	25	110
11/9/1997	19:07	42.8543	12.9998	2	106	13	−148
12/31/1997	16:02	42.8523	13.0235	5.4	328	36	−58

the largest considered distances (i.e. 25–30 km) the mean coherence value is 0.5, i.e. still much higher than the value predicted for unrelated faults. The half-wavelength has a constant value of 7 km for both 2-D and 3-D distances. Another observed cyclicity has a shorter half-wavelength of about 1 km and is particularly evident in the 7–14 km interval. In this case, it is not clear whether it can be considered a secondary natural wavelength train superimposed onto the primary cyclicity or, alternatively, a processing artefact. The histogram of coherence distributions in the maximum coherence zone (less than 3 km separation) indicates a coherent population (Fig. 11c), while earthquake pairs with separations of 6–9 km are incoherent and anti-coherent, returning to a coherent– incoherent distribution for distances of 12–15 km. Because the Kruskal Wallis test result indicates that it is very unlikely that the three sets derive from a single population (Table 2), Kolmogorov–Smirnov and Mann–Whitney tests may be applied: these tests produce high probabilities of equivalence between the coherence distribution of close- and wide separation distances, while that of intermediate separation distances differs markedly from these two distributions (Table 3).

The map representing fault pairs with coherence lower than −1.2 shows that anti-coherent fault pairs are distributed in all portions of the seismogenic zone (Fig. 11d).

4.2.2. Extensional mesofault populations in the Valnerina area

Normal macrofaults in the Valnerina sector trend NW–SE to N–S, with movements towards the SW (Fig. 12a–c). The sub-

parallelism observed in the map between normal and thrust faults could be due to a partial reactivation of the thrust ramps during the Plio-Pleistocene extensional phase.

The normal mesofaults compatible with a SW–NE to E–W extension dip towards the W and present normal-sinistral movements (Fig. 13a). These mesofaults are attributed to the post-orogenic extensional phase on the basis of their geometric characteristics only and some may actually be pre-orogenic normal mesofaults (cf. Scisciani et al., 2002).

Due to the quite low number of data, the coherence diagram is not defined in the 3–7 km distance interval (Fig. 13b). The moving average line and the frequency distributions for three different distance ranges may be compatible with the presence of a spatial cyclicity, having a mean coherence minimum in the 2–7 km interval and a slight increase in mean coherence values for distances greater than 7 km (Fig. 13b and c). The Kruskal Wallis test assigns a very low probability to the null hypothesis of equivalence between three defined intervals of separation (0–1, 2–3 and 7–8 km; see Table 2). According to the Kolmogorov–Smirnov test, the intermediate-separation and wide-separation pairs are probably equivalent, while the close-separation distribution is almost surely different from that of the other two (Table 3).

4.2.3. Contractional mesofault population in the Valnerina area

The reverse mesofault population, of probable Miocene age, is distributed along the Tassinare and Grotti reverse-dextral
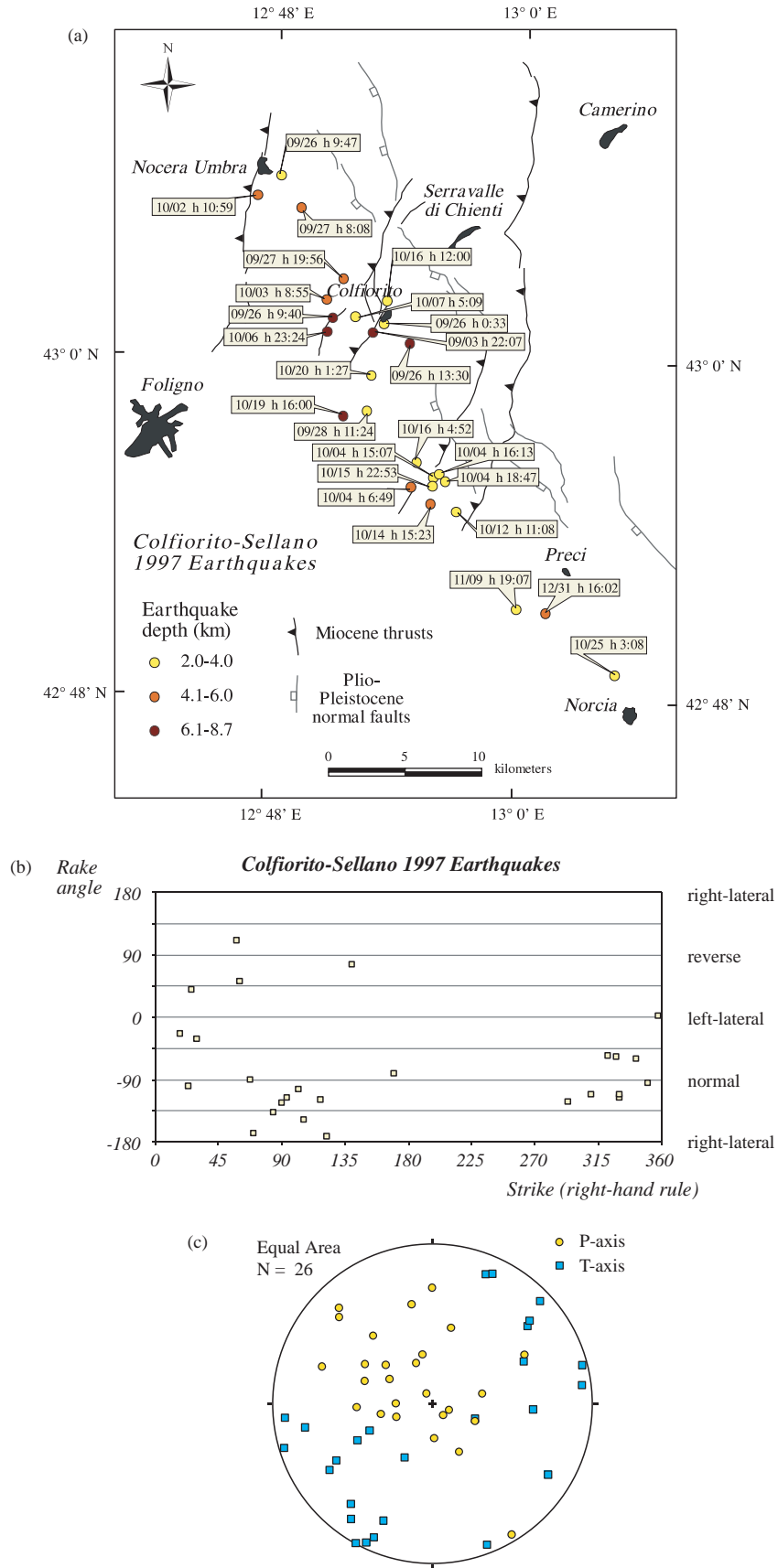
Fig. 10. Colfiorito–Sellano 1997 earthquake data set derived from Cattaneo et al. (2000): (a) earthquake location maps, with fault traces redrawn from figs. 3 and 6 in Chiaraluce et al. (2005); (b) strike vs. rake angle diagram: note the presence of strike-slip and reverse faults together with predominant normal-oblique faults; (c) stereonet of P–T axes indicating predominant low-angle NE–SW extension and sub-vertical to sub-horizontal NW–SE shortening.
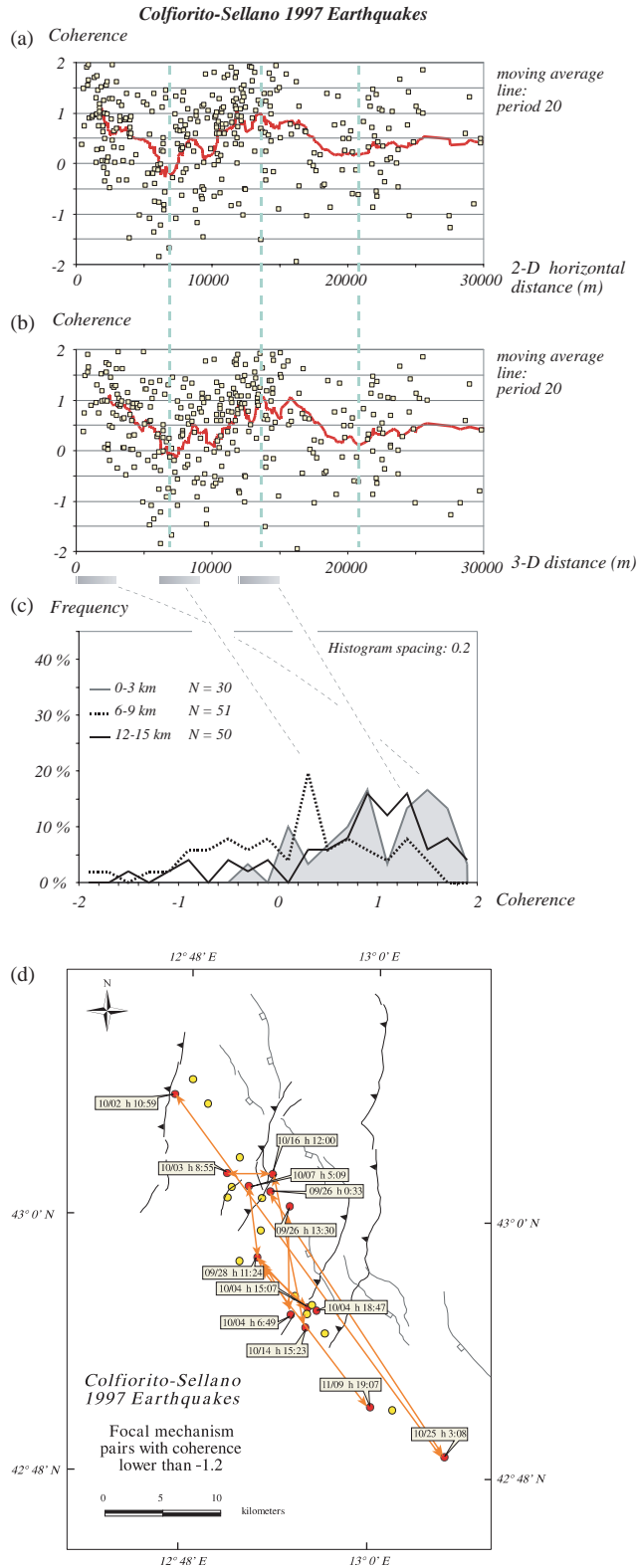
Fig. 11. Coherence spatial analysis of the Colfiorito–Sellano 1997 earthquake data set: (a) scatter diagram of coherence vs. 2D/horizontal distance between earthquake pairs, with moving average line; (b) scatter diagram of coherence vs. 3D-distance, with moving average line, note the vertical bars representing the three identified minimum and maximum mean coherence values; (c) coherence frequency histograms of three distance slices, corresponding to the first maximum (0–3 km), the first minimum (6–9 km), and the second relative maximum (12–15 km): note that earthquake correlation is greater at 12–15 km than at 6–9 km separation; (d) location map of fault traces (redrawn from Chiaraluce et al., 2005, figs. 3 and 6) and earthquake pairs with coherence lower than −1.2: arrows connect each couple.

Table 2
Separation ranges used for the separation-derived subsets of Colfiorito–Sellano 1997 earthquake and Valnerina mesofault data sets (left) and probabilities for the null hypothesis of their belonging to a population with a constant median, as derived from the Kruskal Wallis statistical test (right). The very low statistical significance favours the rejection of the null hypothesis for all natural data sets

Set	Separations			Kruskal Wallis Asymp. Sig.
	(1) Near-separation range	(2) Intermediate separation range	(3) Far-separation range	
Colfiorito–Sellano 1997 earthquakes	0–3 km ($N=30$)	6–9 km ($N=51$)	12–15 km ($N=50$)	1.53E−06
Valnerina—normal mesofaults	0–1 km ($N=57$)	2–3 km ($N=22$)	7–8 km ($N=22$)	1.11E−14
Valnerina—reverse mesofaults	0–2 km ($N=296$)	3.5–5.5 km ($N=242$)	7–9 km ($N=249$)	8.90E−12
Valnerina—mesofaults along Grotti macrofault	0–2 km ($N=188$)	2–4 km ($N=164$)	6–8 km ($N=50$)	8.32E−43

Table 3
Results of statistical analyses (Kolmogorov–Smirnov and Mann–Whitney) performed on the natural data sets, split into three separation subsets according to values listed in Table 2

Set	Kolmogorov–Smirnov Asymp. Sig. (2-tailed)			Mann–Whitney Asymp. Sig. (2-tailed)		
	(1) vs. (2)	(1) vs. (3)	(2) vs. (3)	(1) vs. (2)	(1) vs. (3)	(2) vs. (3)
Colfiorito–Sellano 1997 Earthquakes	2.09E−05	6.26E−01	2.22E−04	2.21E−06	2.33E−01	8.16E−05
Valnerina—normal mesofaults	0.00E+00	4.17E−07	5.00E−02	8.16E−12	1.47E−08	7.45E−03
Valnerina—reverse mesofaults	0.00E+00	6.69E−01	0.00E+00	8.90E−12	8.09E−01	1.36E−11
Valnerina—mesofaults along Grotti macrofault	0.00E+00	4.38E−04	0.00E+00	1.43E−39	3.12E−03	1.66E−17

macrofaults and in their footwalls (Fig. 14a). This population consists of a more developed set of W-dipping reverse-dextral faults and a second, less developed set of E-dipping conjugate reverse-sinistral faults (Fig. 14b).

The coherence distribution ranges from 2.0 to −1.0, with no values lower than –1.0 (Fig. 14c and d). Although the distance relationships are not well structured, it is possible to identify, following the initial maximum of mean coherence, a minimum
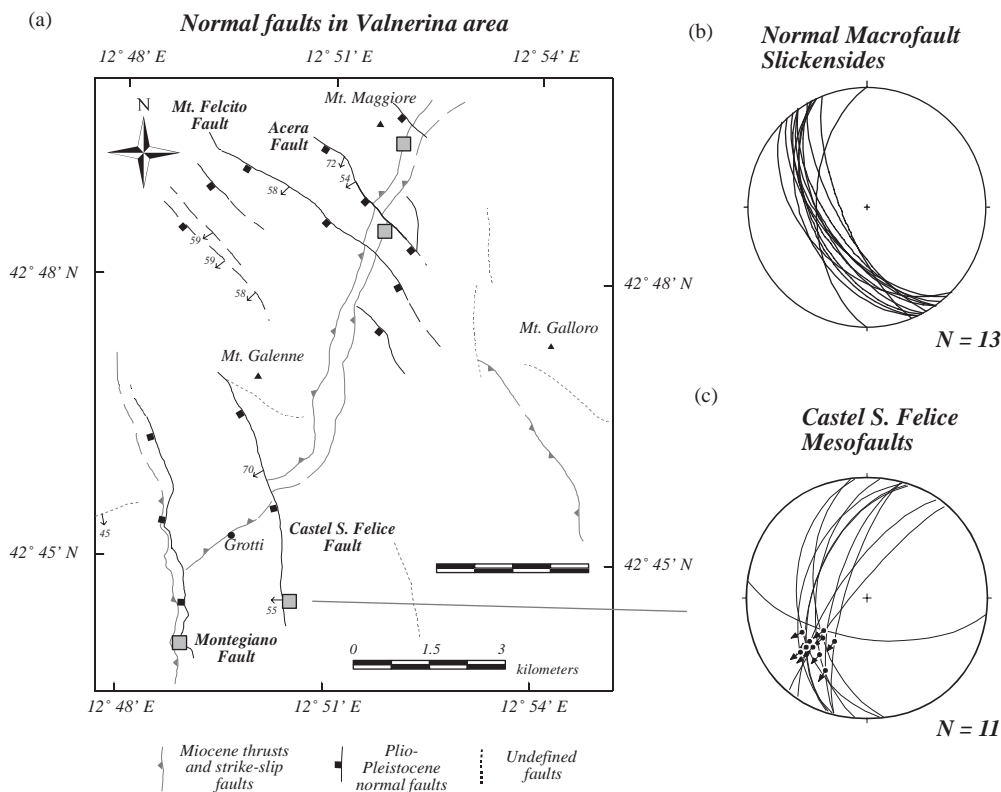

Fig. 12. Normal faults in the Valnerina area: (a) structural sketch and location of sampled normal mesofaults (grey squares); (b) stereonet of normal macrofault slickensides (mainly from Acera, Mt. Felcito and Castel S. Felice Faults and from areas in between); (c) stereonet of striae on mesofault planes sampled along the Castel S. Felice Fault, showing normal/left-lateral movements.
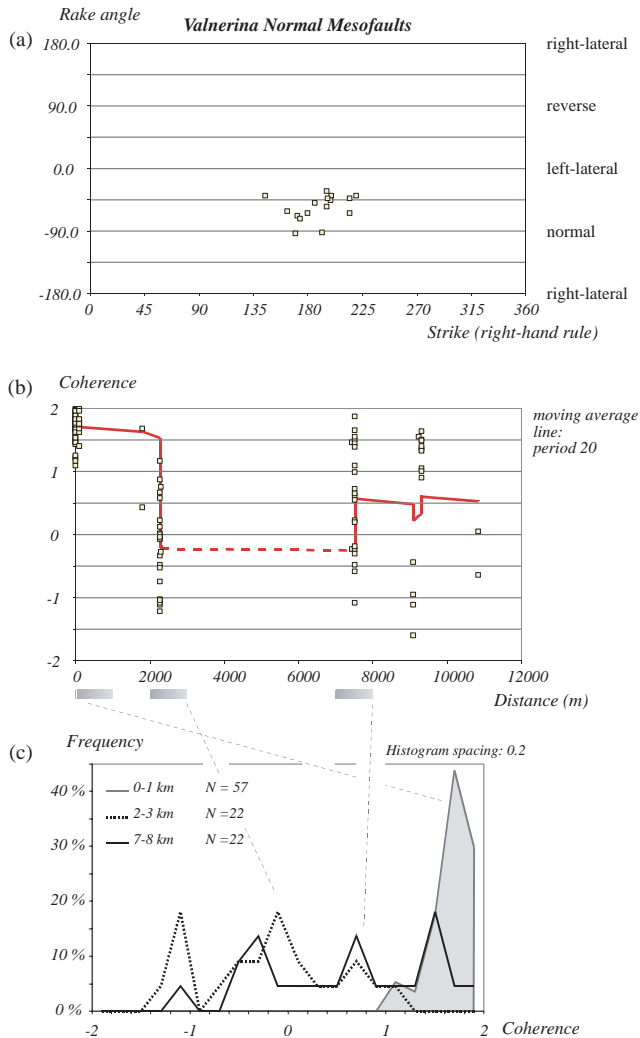
Fig. 13. Normal mesofaults in the Valnerina area: (a) strike vs. rake angle plot: mesofaults are normal to normal/left-lateral and strike from SE to SW; (b) scatter diagram of coherence vs. horizontal distance between fault pairs, with moving average line: note the poorly constrained minimum interval between 3 and 7 km; (c) coherence frequency histograms of three distance slices corresponding to the first maximum (0–1 km), the initial part of the possible minimum (2–3 km), the transition to a second relative maximum (7–8 km). Coherence values at short distances are higher than those at intermediate distances and long distances.

revealed by the structure contour map and by the corresponding mesofault populations with alternate reverse-oblique and normal-oblique movements (Fig. 15a). These relationships suggest that folding of the macrofault planar surface occurred during or shortly after its activity, even if an original bent macrofault attitude cannot be ruled out. The mesofault coherence distribution presents a spatial cyclicity, with coherent fault pairs for distances of less than 2 km, a mean coherence minimum in the 2–4 km interval, with anti-coherent and incoherent pairs, and a secondary maximum for fault pairs more than 6–8 km apart, with a predominance of coherent pairs (Fig. 16a–c). In all likelihood the fault pair sets do not derive from a single population (Table 2) but differ from each other, as evidenced by both the Kolmogorov–Smirnov and the Mann–Whitney tests (Table 3).

5. Discussion

5.1. Slip tendency distribution in natural data sets

The analysis of coherence distributions in natural data sets may provide some insight into the role of slip tendency in fault formation and activity. When comparing the distributions for short-range fault/earthquake pairs (especially within the first km of separation), it is possible to note that most data, both for present-day earthquakes (Fig. 11a–c), Plio-Pleistocene normal faults (Fig. 13b and c) and for Miocene mainly reverse-oblique faults (Figs. 14c and d and 16b and c), fall into the 0.5–2.0 coherence interval, i.e. earthquakes/faults tend to be very correlated with each other. This implies that only potential surfaces with high slip tendency (i.e. higher than the second–third quartile of all potential surfaces) will actually develop and/or evolve as faults, inhibiting the formation of less well-oriented potential faults.

The actual determination of the slip tendency for natural data sets is beyond the scope of this study. Assuming that a fault population originated from a stress field with constant Φ value, and given a statistically representative data set, one possible way to find the best slip tendency value involves comparing theoretical cumulative curves for various Φ values with the observed cumulative distribution.

5.2. Spatial structure of fault populations and genetic mechanisms

As evidenced by both coherence-separation diagrams (Figs. 11, 13, 14 and 16) and statistical tests (Tables 2 and 3), present-day earthquakes and Miocene reverse-oblique mesofaults from the analysed Umbria–Marche sectors tend to show spatial cyclicities: highly correlated fault/earthquake pairs for short distances (0–2 km), poorly correlated pairs for intermediate distances (7 km for Colfiorito earthquakes and 3–6 km for Valnerina faults) and again well-to-medium correlated pairs for longer distances (14 km in Colfiorito and 7–9 km in Valnerina).

in the 4–5 km interval and a subsequent slow increase for larger distances. As for the previous data sets, fault pairs separated by short and long distances are more highly correlated than intermediate distance pairs (Fig. 14d). As the null hypothesis of equivalence between the three subsets is rejected by the Kruskal Wallis test (Table 2), the Kolmogorov–Smirnov and the Mann–Whitney tests were applied: close-separation and wide-separation pair distributions display a very high probability of equivalence, while the intermediate-separation pair distribution is unlike that of the other two distributions (Table 3).

Mesofault populations distributed in the Grotti macrofault zone (Fig. 15a and b) show a somewhat similar situation. The macrofault presents strike variations along its direction, as
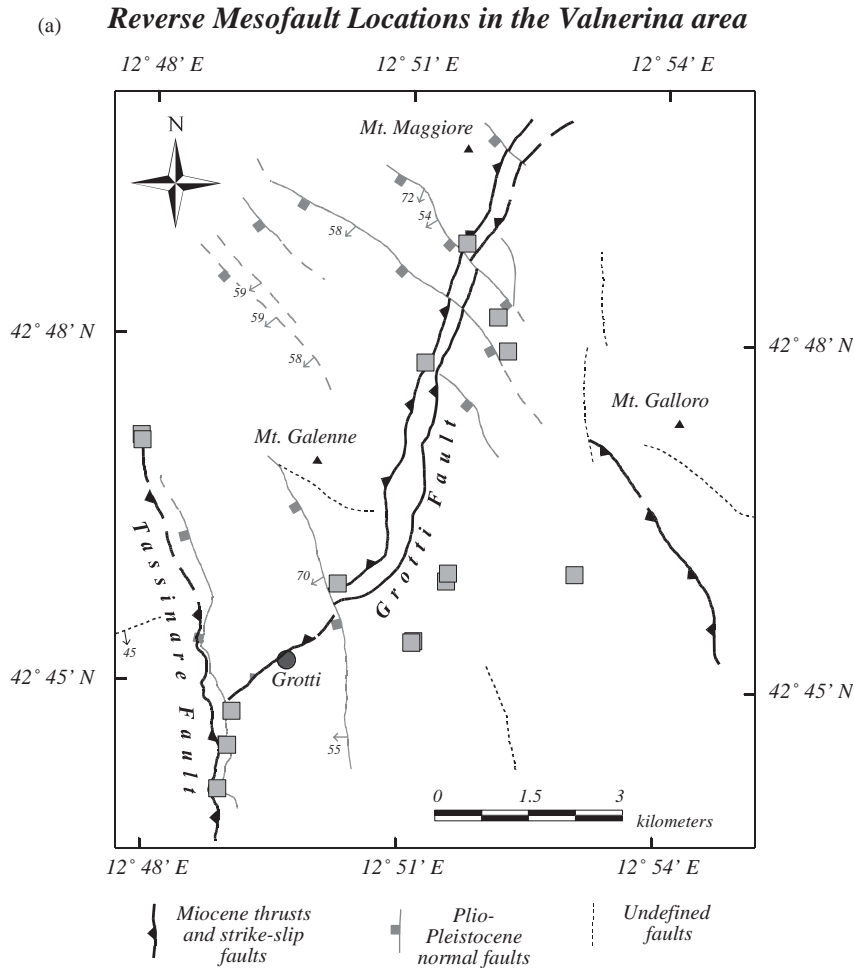
Fig. 14. Reverse mesofaults in Valnerina area: (a) Structural sketch and locations of the sampled Miocene reverse mesofaults (grey squares), distributed mainly along Tassinare and Grotti Faults and in their footwalls; (b) strike vs. rake angle plot: the data set consists of a S-striking set with reverse-dextral movements and a conjugate N-striking set with reverse-left-lateral movements; (c) scatter diagram of coherence vs. horizontal distance between fault pairs, with moving average line: a minimum of mean values lie in the 3–5 km interval; (d) coherence frequency histograms of three distance slices corresponding to the first maximum (0–2 km), the core of the minimum zone (3.5–5.5 km), and a secondary maximum (7–9 km): coherence values are higher in short and long distance slices than in intermediate distance slices.

The details of variations, however, differ from data set to data set. In the case of earthquakes and reverse mesofaults, the presence of a periodicity is confirmed by the Kolmogorov–Smirnov and Mann–Whitney tests, because no statistical difference in coherence distributions is found for short and long distances, while the coherence distribution of intermediate separation distances differs from that of the other two subsets (Tables 2 and 3). For the mesofaults along the reverse Grotti fault, the Kolmogorov–Smirnov and Mann–Whitney tests favour the hypothesis of three different sets for the three increasing separation intervals (Table 3): however, the coherence-separation diagram and the three derived distributions highlight how the mean, calculated for at least six different separation values, tends to decrease and then increase (Fig. 16b and c).

The case of Valnerina normal mesofaults is quite different: the data appear to be spatially under-sampled (with only four different separation values; see Fig. 13b) and both the

histograms of coherence distribution (Fig. 13c) and statistical tests (Table 3) display a certain degree of similarity between intermediate distance and longer distances sets. In this case, a more uniform and dense spatial distribution of data would allow the unambiguous determination of possible spatial cyclicities.

In the case of the 1997 Colfiorito–Sellano earthquake, the focal mechanisms responsible for such cyclicity could hardly be considered just local outliers, since they are distributed in all subareas of the seismogenic region (Fig. 11d). On the other hand, the well-defined spatial structures evident in Fig. 11a and b seem incompatible with the mere presence of random errors. The fact that the wavelength is unaffected by the change from a 2-D to a 3-D distance suggests the predominance of horizontal factors in genetic mechanisms. Normal fault segments in the seismogenic region have a mean length of 5–10 km (Chiaraluce et al., 2004), so that mechanical interaction between segments (causing stress axis reorientations) should give rise to
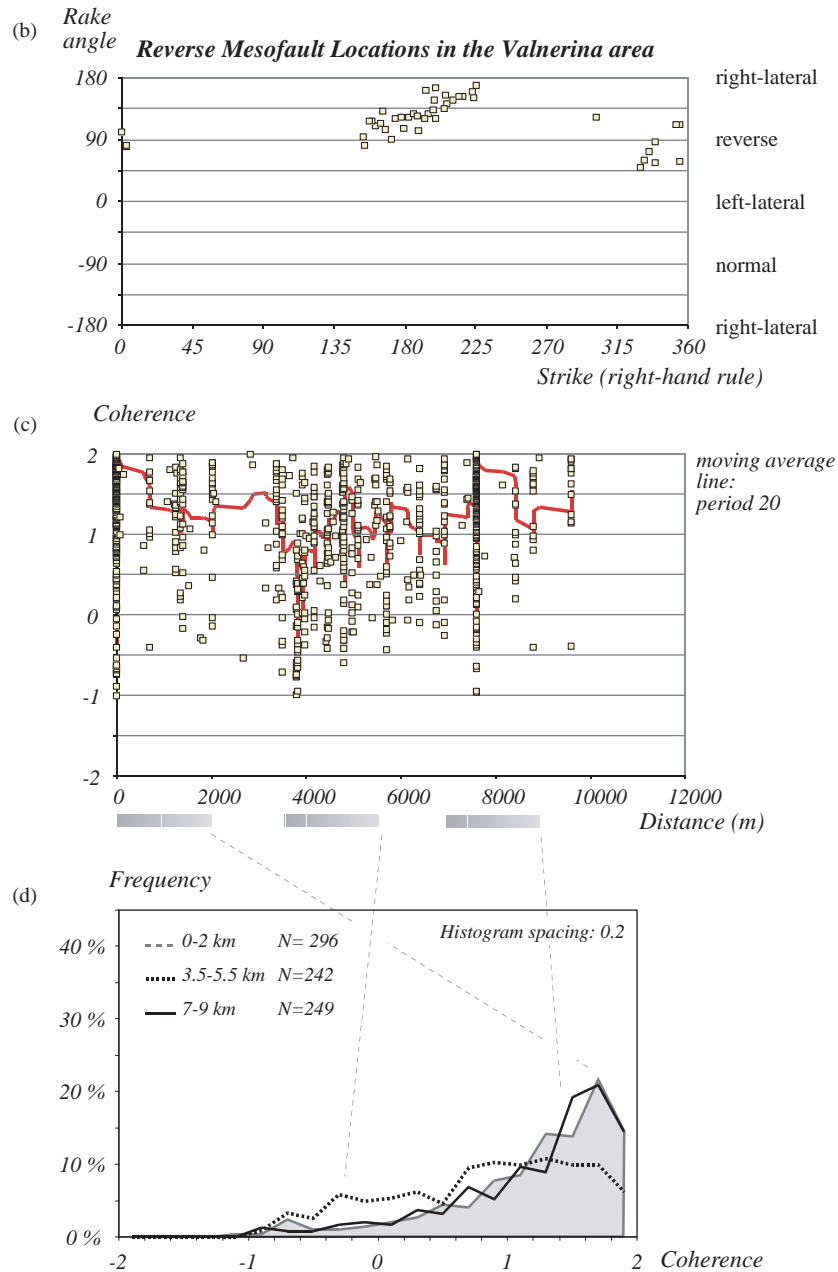
Fig. 14 (*continued*)

a wavelength that is just half of that observed one. One possible interpretation is that the cyclicity is controlled by the thrust structure inherited from the previous Miocene compressive phase: indeed, the mean spacing between the major pre-existing thrust zones in a NNW–SSE direction is about 15 km (figs. 3 and 6 in Chiaraluce et al., 2005; see also Fig. 11d for a comparison with the locations of worst-paired earthquakes). This interpretation is in agreement with Chiaraluce et al. (2004, 2005), who state that the present-day strike-slip events occur along inherited structures.

The derived spatial wavelength (7–9 km) for coherence from the Valnerina contractional mesofaults is consistent with the observed macrofold wavelengths (mean value of around 8 km; compare cross-sections A and B in Fig. 15b). This fact

suggests that these mesofaults experienced syn- to post-thrusting folding processes (cf. Koopman, 1983), which produced the periodic fluctuations in coherence values.

In summary, the observed spatial cyclicities in the 1997 Colfiorito earthquakes and the Valnerina reverse mesofaults suggest that fault characteristics may be controlled or modified by spatially-periodic factors with a wavelength of the order of many km. This finding is not surprising: both theoretical and experimental studies indicate that the orientation of new faults may be markedly influenced by pre-existing mechanical anisotropies or planes of weakness (e.g. Jaeger, 1960; Donath, 1961).

Based on the investigated natural data sets, at least in the 10^1–10^2 km distance range, the natural decay of mean
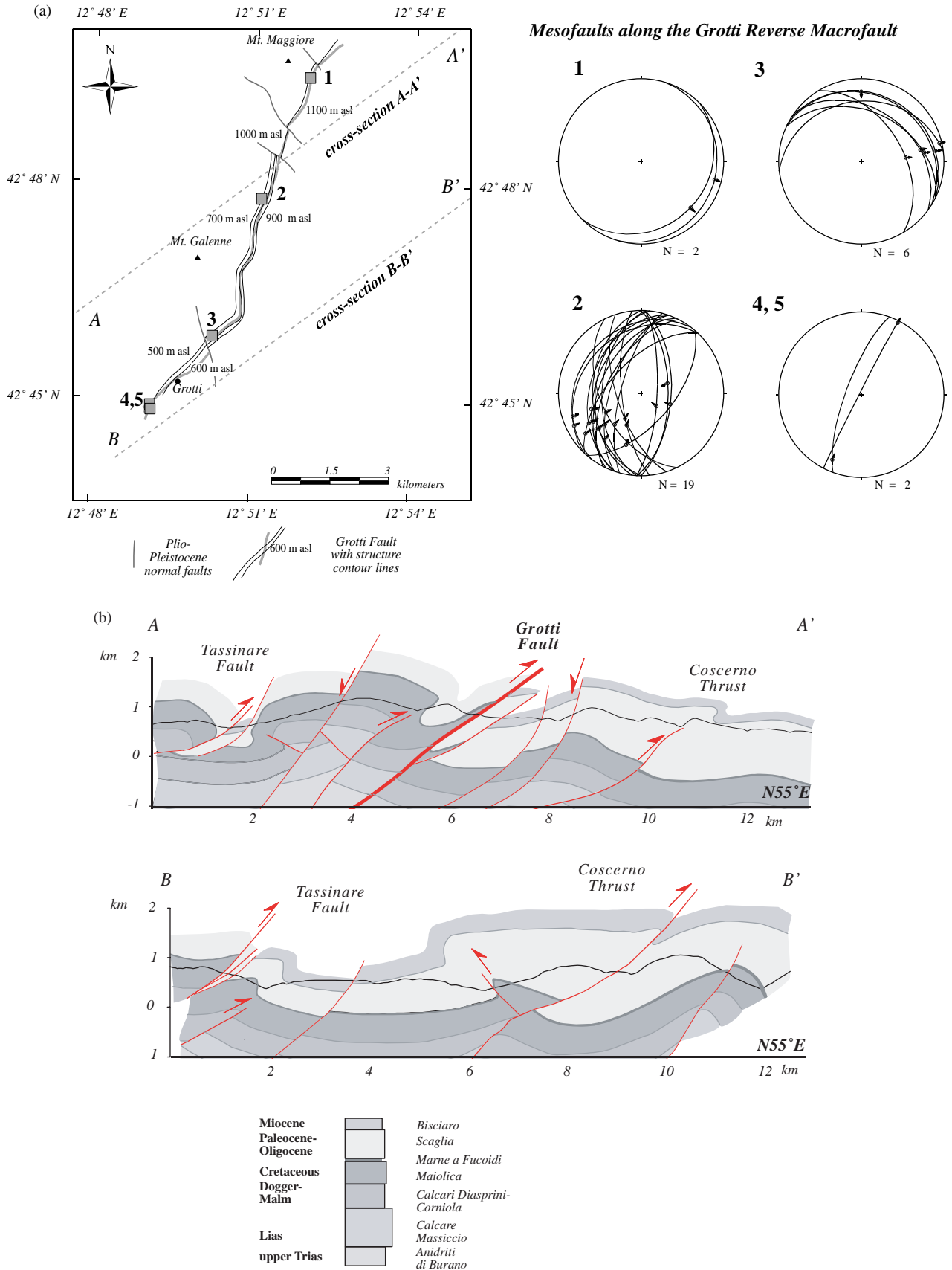
Fig. 15. Mesofaults along the reverse-dextral Grotti macrofault: (a) structural contour map of the Grotti Fault, with cross-section traces and mesofault sampling locations (numbered grey squares); stereonets of mesofaults in the sampled sites to the right: note the large variations in mesofault plane orientations and striae movement directions at different sites; (b) cross-sections along the two traces: the mean macro-fold wavelength is around 8 km.
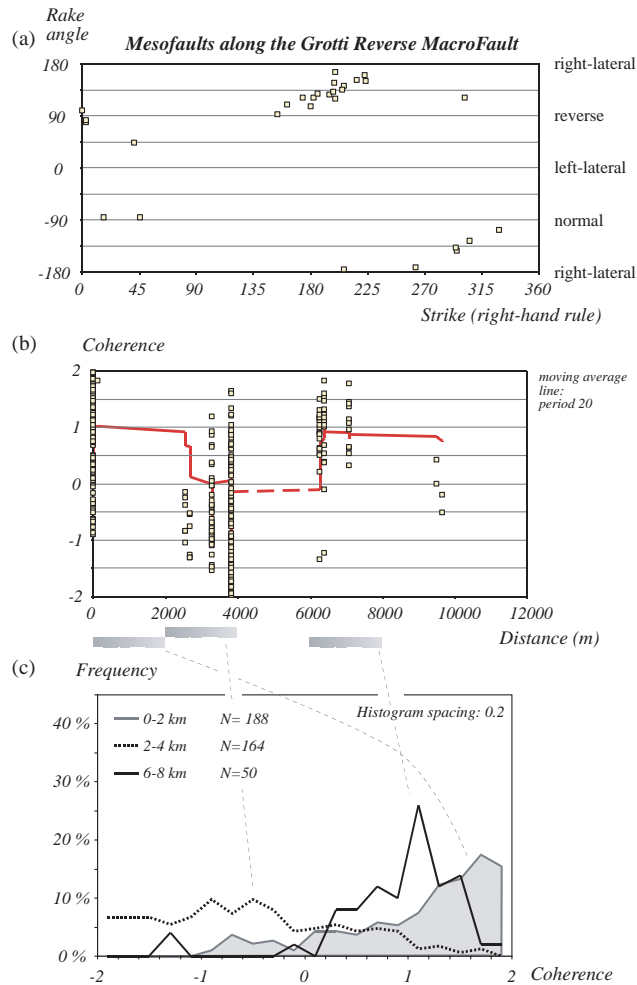
Fig. 16. Coherence spatial analysis of mesofaults along the reverse-dextral Grotti macrofault: (a) strike vs. rake angle plot: strike and movement types are quite varied, and include reverse and normal movements; (b) scatter diagram of coherence vs. horizontal distance between fault pairs, with moving average line: after the first maximum for short distances, there is a minimum at around 2–4 km and a maximum at 6–8 km; (c) coherence frequency histograms of three distance slices for the two relative maxima and the intermediate minimum.

coherence with increasing distance can differ from the 'normal' monotonically-decreasing model of Kagan and Knopoff (1985b) and Kagan (1992a) (see Fig. 8), with the presence of periodicities both in earthquakes and in faults. On the other hand, the results of the random fault simulation fit very well with the experimentally-observed mean and standard deviation of coherence for faults more than 10^4 km apart of Kagan and Knopoff (1985b) and Kagan (1992a) (compare Figs. 7 and 8).

5.3. Coherence and stress field

The simulation of a homogeneous stress field indicates that, when dealing with monophase fault populations, coherence distributions should mainly fall in the 0.0–2.0 interval, especially if the slip tendency of faults is high (Fig. 4).

For faults that originated in a stress field with Φ variations, simulations reveal a limited influence on coherence distributions (Fig. 5), while rotations of σ_1 and σ_3 axes tend to significantly reduce coherence values

(Fig. 6). Totally unrelated fault data sets are characterized by a zero mean value of coherence, with a symmetric distribution around the mean, and a standard deviation of 0.9 (Fig. 7). Distributions similar to the unrelated one are produced by 45–60° spatial or temporal rotations of σ_1 and σ_3 stress axes, depending on the Φ value and/or on the slip tendency distribution of active faults (Fig. 6). Larger rotations produce anti-correlated distributions.

We applied the diagrams derived for cases of stress field variations (Figs. 5 and 6) to the 1997 Colfiorito–Sellano earthquake data set as an example because pre-existing planes, whose impact on coherence variations was not treated theoretically in this study, were found to influence stress fields. The mean coherence decreases by about 1.5 over a distance of 7 km: stress axis rotations that could originate such a decrease range from 20–30° (considering a substantial Φ variation contribution) to 50–60° (without Φ variation contribution). Since simulations do not consider the case of all three axis rotations coupled with stress ratio variations, the theoretically required stress rotation could be

significantly lower than 50–60° degrees. The interplay between pre-existing structures and stress reorientations could account for the strike-slip and especially reverse focal mechanisms observed by Cattaneo et al. (2000) and Chiaraluce et al. (2004, 2005).

6. Conclusions

The proposed method represents an extension to fault data of the coherence method of Kagan and Knopoff (1985a,b), originally devised for spatial analysis of earthquakes. Coherence is a tensor-derived measure of the similarity between two faults or earthquakes. It can be automatically calculated for geo-referenced mesofault populations through the use of a customized GIS routine, which analyses the resulting distribution as a function of the distance and angular offset between pairs.

The analysis of natural earthquake and fault data sets from the Umbria–Marche region (Italy), currently undergoing extension after a Miocene compressive phase and older extensional phases, reveals cyclic spatial structures in the coherence of both present-day earthquakes and Miocene reverse-oblique meso- and macro-faults.

In the case of Miocene faults, the observed cyclicity could be explained by compressive syn- to post-faulting folding. For the recent earthquakes, pre-existing Miocene compressive structures may have induced stress field reorientations.

The analysis of this polyphase terrain thus confirms that the spatial structure of earthquake and fault populations can be controlled by the spatial characteristics of older structures such as folds and faults.

Acknowledgements

The customized ArcView® 3.1 GIS project is available from the author upon request.

Appendix A. Fault Cartesian components and fault moment tensor calculation

Fault data are generally expressed as the right-hand rule strike (ς, 0–360°) and/or dip-direction ($\varphi = \varsigma + 90°$, 0–360°) of the fault plane and its dip angle (δ, 0–90°), while the movement direction is expressed as trend (α, 0–360°) and plunge (β, from $-90°$ to $+90°$, with upward-directed negative values) or as rake angle (λ, $-180°$ to $+180°$). To avoid ambiguity, the fault normal must lie in the rock volume containing the vector product of dip-direction and the right-hand rule strike vectors, with the movement vector referring to that rock volume. Negative plunge expresses upward (reverse) movement.

According to convention (Aki and Richards, 1980, Eq. 4.83; Kagan, 1991, Eqs. 8 and 9; Cladouhos and Allmendinger, 1993, Eqs. A1 and A2), the components of the fault normal (**v**) and slickenline (**u**) unit vectors in a North (x)–East (y)–Down (z) orthonormal vector system are found in Table A1.

The calculation of $M_{ij}^* = \frac{1}{2}(u_i v_j + u_j v_i)$ using the right-hand rule strike and rake angle convention gives (Aki and Richards, 1980, vol. I, Box 4.4):

$$M_{xx}^* = -0.5\sin(\delta)\cos(\lambda)\sin(2\varsigma)$$
$$- 0.5\sin(2\delta)\sin(\lambda)\sin^2(\varsigma) \tag{A1}$$

$$M_{xy}^* = M_{yx}^* = 0.5\sin(\delta)\cos(\lambda)\cos(2\varsigma)$$
$$+ 0.25\sin(2\delta)\sin(\lambda)\sin(2\varsigma) \tag{A2}$$

$$M_{xz}^* = M_{zx}^* = -0.5\cos(\delta)\cos(\lambda)\cos(\varsigma)$$
$$- 0.5\cos(2\delta)\sin(\lambda)\sin(\varsigma) \tag{A3}$$

$$M_{yy}^* = 0.5\sin(\delta)\cos(\lambda)\sin(2\varsigma) - 0.5\sin(2\delta)\sin(\lambda)\cos^2(\varsigma) \tag{A4}$$

$$M_{yz}^* = M_{zy}^* = -0.5\cos(\delta)\cos(\lambda)\sin(\varsigma)$$
$$+ 0.5\cos(2\delta)\sin(\lambda)\cos(\varsigma) \tag{A5}$$

$$M_{zz}^* = 0.5\sin(2\delta)\sin(\lambda) \tag{A6}$$

Table A1

	Right-hand rule strike (ς) Trend (α) and plunge (β) (Cladouhos and Allmendinger, 1993)	Dip-direction (φ) Trend (α) and plunge (β)	Right-hand rule strike (ς) Rake angle (λ) (Aki and Richards, 1980)	Dip-direction (φ) Rake angle (λ) (Kagan, 1991)
v_x	$-\sin(\delta)\sin(\varsigma)$	$\sin(\delta)\cos(\varphi)$	$-\sin(\delta)\sin(\varsigma)$	$\sin(\delta)\cos(\varphi)$
v_y	$\sin(\delta)\cos(\varsigma)$	$\sin(\delta)\sin(\varphi)$	$\sin(\delta)\cos(\varsigma)$	$\sin(\delta)\sin(\varphi)$
v_z	$-\cos(\delta)$	$-\cos(\delta)$	$-\cos(\delta)$	$-\cos(\delta)$
u_x	$\cos(\alpha)\cos(\beta)$	$\cos(\alpha)\cos(\beta)$	$\cos(\lambda)\cos(\varsigma) + \sin(\lambda)\cos(\delta)\sin(\varsigma)$	$\sin(\lambda)\sin(\varphi) - \sin(\lambda)\cos(\delta)\cos(\varphi)$
u_y	$\sin(\alpha)\cos(\beta)$	$\sin(\alpha)\cos(\beta)$	$\cos(\lambda)\sin(\varsigma) - \sin(\lambda)\cos(\delta)\cos(\varsigma)$	$-\cos(\lambda)\cos(\varphi) - \sin(\lambda)\cos(\delta)\sin(\varphi)$
u_z	$\sin(\beta)$	$\sin(\beta)$	$-\sin(\lambda)\sin(\delta)$	$-\sin(\lambda)\sin(\delta)$

Appendix B. Rotation matrix

Vectors, matrices and tensors can be rotated around a pole using matrix multiplication (e.g. Kagan and Knopoff, 1985a, p. 433; Cox and Hart, 1986, pp. 226–227; Angelier, 2002, p. 593).

Given the rotation pole (with direction cosines l, m, n) and the rotation angle (ρ, $-180°$ to $+180°$), the rotation matrix R components are (Kagan and Knopoff, 1985a, Eq. 5, p. 433, but note the error in the value of the R_{21} component; Cox and Hart, 1986, p. 227):

$$R_{11} = l^2(1-\cos\rho) + \cos\rho \tag{B1}$$

$$R_{12} = lm(1-\cos\rho) - n\sin\rho \tag{B2}$$

$$R_{13} = ln(1-\cos\rho) + m\sin\rho \tag{B3}$$

$$R_{21} = lm(1-\cos\rho) + n\sin\rho \tag{B4}$$

$$R_{22} = m^2(1-\cos\rho) + \cos\rho \tag{B5}$$

$$R_{23} = mn(1-\cos\rho) - l\sin\rho \tag{B6}$$

$$R_{31} = ln(1-\cos\rho) - m\sin\rho \tag{B7}$$

$$R_{32} = mn(1-\cos\rho) + l\sin\rho \tag{B8}$$

$$R_{33} = n^2(1-\cos\rho) + \cos\rho \tag{B9}$$

References

Aki, K., Richards, P.G., 1980. Quantitative Seismology. Theory and Methods. Vol. I. W.H. Freeman and Company, San Francisco.

Albarello, D., 2000. A resampling approach to test stress-field uniformity from fault data. Geophysical Journal International 140, 535–542.

Alberti, M., 2005. Application of GIS to spatial analysis of mesofault populations. Computers & Geosciences 31,1249–1259, doi:10.1016/j.cageo.2005.03.013.

Amato, A., Azzara, R., Chiarabba, C., Cimini, G.B., Cocco, M., Di Bona, M., Margheriti, L., Mazza, S., Mele, F., Selvaggi, G., Basili, A., Boschi, E., Courboulex, F., Deschamps, A., Gaffet, S., Bittarelli, G., Chiaraluce, L., Piccinini, D., Ripepe, M., 1998. The 1997 Umbria–Marche, Italy, earthquake sequence: a first look at the main shocks and aftershocks. Geophysical Research Letters 25, 2861–2864.

Angelier, J., 2002. Inversion of earthquake focal mechanisms to obtain the seismotectonic stress IV—a new method free of choice among nodal planes. Geophysical Journal International 150, 588–609.

Angelier, J., Mechler, P., 1977. Sur une méthode graphique de recherché des contraintes principales également utilisable en tectonique et en seismologie: la méthode des diédres droits. Bulletin de la Sociètè Géologique France 19, 1309–1318.

Baldanza, A., Colacicchi, R., Parisi, G., 1982. Controllo tettonico sulla deposizione dei livelli detritici nella Scaglia Cretaceo–Paleocenica (Umbria Orientale). Rendiconti Società Geologica Italiana 5, 11–14.

Boncio, P., Lavecchia, G., 2000. A geological model for the Colfiorito earthquakes (September–October 1997, central Italy). Journal of Seismology 4, 345–356.

Bott, M.H.P., 1959. The mechanics of oblique slip faulting. Geological Magazine 96, 109–117.

Cattaneo, M., Augliera, P., De Luca, G., Gorini, A., Govoni, A., Marcucci, S., Michelini, A., Monachesi, G., Spallarossa, D., Troiani, L., XGUMS, 2000. The 1997 Umbria–Marche (Italy) earthquake sequence: analysis of the data recorded by the local and temporary networks. Journal of Seismology 4, 401–414.

Célérier, B., Seranne, M., 2001. Breddin's graph for tectonic regimes. Journal of Structural Geology 23, 789–801.

Channell, J.E.T., 1992. Paleomagnetic data from Umbria (Italy): implications for the rotation of Adria and Mesozoic apparent polar wander paths. Tectonophysics 216, 365–378.

Cheeney, R.F., 1983. Statistical Methods in Geology for Field and Lab Decisions. George Allen & Unwin, London.

Chiaraluce, L., Amato, A., Cocco, M., Chiarabba, C., Selvaggi, G., Di Bona, M., Piccinini, D., Deschamps, L., Margheriti, F., Courboulex, F., Ripepe, M., 2004. Complex normal faulting in the Apennines thrust-and-fold belt: the 1997 seismic sequence in Central Italy. Bulletin of the Seismological Society of America 94, 99–116.

Chiaraluce, L., Barchi, M., Collettini, C., Mirabella, F., Pucci, S., 2005. Connecting seismically active normal faults with Quaternary geological structures in a complex extensional environment: the Colfiorito 1997 case history (northern Apennines, Italy). Tectonics 24, TC1002. doi:10.1029/2004TC001627.

Cladouhos, T.T., Allmendinger, R.W., 1993. Finite strain and rotation from fault-slip data. Journal of Structural Geology 15, 771–784.

Cox, A., Hart, R.B., 1986. Plate Tectonics: How it Works. Blackwell Scientific Publications, Palo Alto, California.

Cressie, N.A.C., 1993. Statistics for Spatial Data. John Wiley & Sons, New York.

Decandia, F.A., 1982. Geologia dei Monti di Spoleto (Provincia di Perugia). Bollettino Società Geologica Italiana 101, 291–315.

Donath, F.A., 1961. Experimental study of shear failure in anisotropic rocks. Geological Society of America Bulletin 72, 985–990.

Ekström, G., Morelli, A., Boschi, E., Dziewonski, A.M., 1998. Moment tensor analysis of the central Italy earthquake sequence of September–October 1997. Geophysical Research Letters 25, 1971–1974.

Gillard, D., Wyss, M., 1995. Comparison of strain and stress tensor orientation: application to Iran and southern California. Journal of Geophysical Research 100 (B11), 22197–22213.

Hardcastle, K.C., Hills, L.S., 1991. BRUTE3 and SELECT: Quickbasic 4 programs for determination of stress tensor configurations and separation of heterogeneous populations of fault-slip data. Computers & Geosciences 17, 23–43.

Jaeger, J.C., 1960. Shear failure of anisotropic rocks. Geological Magazine 97, 65–72.

Kagan, Y.Y., 1991. 3-D rotation of double-couple earthquake sources. Geophysical Journal International 106, 709–716.

Kagan, Y.Y., 1992a. On the geometry of an earthquake fault system. Physics of the Earth and Planetary Interiors 71, 15–35.

Kagan, Y.Y., 1992b. Correlations of earthquake focal mechanisms. Geophysical Journal International 110, 305–320.

Kagan, Y.Y., 2000. Temporal correlation of earthquake focal mechanisms. Geophysical Journal International 143, 881–897.

Kagan, Y.Y., Knopoff, L., 1985a. The first-order statistical moment of the seismic moment tensor. Geophysical Journal of the Royal Astronomical Society 81, 429–444.

Kagan, Y.Y., Knopoff, L., 1985b. The two-point correlation function of the seismic moment tensor. Geophysical Journal of the Royal Astronomical Society 83, 637–656.

Knox-Robinson, C.M., Gardoll, S.J., 1998. GIS-stereoplot: an interactive stereonet plotting module for ArcView 3.0 geographic information system. Computers & Geosciences 24, 243–250.

Koopman, A., 1983. Detachment tectonics in the central Apennines, Italy. Geologica Ultraiectina 30, 1–155.

Lavecchia, G., 1985. Il sovrascorrimento dei Monti Sibillini: analisi cinematica e strutturale. Bollettino Società Geologica Italiana 104, 161–194.

Lavecchia, G., Brozzetti, F., Barchi, M., Menichetti, M., Keller, J.V.A., 1994. Seismotectonic zoning in east-central Italy deduced from an analysis of the Neogene to present deformations and related stress fields. Geological Society of America Bulletin 106, 1107–1120.

Marrett, R., Allmendinger, R.W., 1990. Kinematic analysis of fault-slip-data. Journal of Structural Geology 12, 973–986.

Molnar, P., 1983. Average regional strain due to slip on numerous faults of different orientations. Journal Geophysical Research B88, 6430–6432.

Morelli, A., Ekström, G., Olivieri, M., 2000. Source properties of the 1997–98 Central Italy earthquake sequence from inversion of long-period and broad-band seismograms. Journal of Seismology 4, 365–375.

Morris, A., Ferrill, D.A., Henderson, D.B., 1996. Slip-tendency analysis and fault reactivation. Geology 24, 275–278.

Murru, M., Console, R., Lisi, A., 2004. Seismicity and mean magnitude variations correlated to the strongest earthquakes of the 1997 Umbria–Marche sequence (central Italy). Journal of Geophysical Research 109, B01304.

Nemcok, M., Lisle, R.J., 1995. A stress inversion procedure for polyphase fault/slip data sets. Journal of Structural Geology 17, 1445–1453.

Nemcok, M., Kovác, D., Lisle, R.J., 1999. A stress inversion procedure for polyphase calcite twin and fault/slip data sets. Journal of Structural Geology 21, 597–611.

Nieto-Samaniego, A.F., Alaniz-Alvarez, S.A., 1997. Origin and tectonic interpretation of multiple fault patterns. Tectonophysics 270, 197–206.

Oertel, G., 1965. The mechanism of faulting in clay experiments. Tectonophysics 2, 343–393.

Orife, T., Lisle, R.J., 2003. Numerical processing of palaeostress results. Journal of Structural Geology 25, 949–957.

Pardo-Igúzquiza, E., Dowd, P.A., 2004. Normality tests for spatially correlated data. Mathematical Geology 36, 659–681.

Pollard, D.D., Saltzer, S.D., Rubin, A.M., 1993. Stress inversion methods: are they based on faulty assumptions? Journal of Structural Geology 15, 1045–1054.

Reches, Z., 1978. Analysis of faulting in three-dimensional strain field. Tectonophysics 47, 109–129.

Scisciani, V., Tavarnelli, E., Calamita, F., 2002. The interaction of extensional and contractional deformations in the outer zones of the Central Apennines, Italy. Journal of Structural Geology 24, 1647–1658.

Shan, Y., Suen, H., Lin, G., 2003. Separation of polyphase fault/slip data: an objective-function algorithm based on hard division. Journal of Structural Geology 25, 829–840.

Siegel, S., Castellan Jr., N.J., 1988. Nonparametric Statistics for the Behavioral Sciences. McGraw-Hill, New York.

Twiss, R.J., Protzman, G.M., Hurst, S.D., 1991. Theory of slickenline patterns based on the velocity gradient tensor and microrotation. Tectonophysics 186, 215–239.

Twiss, R.J., Souter, B.J., Unruh, J.R., 1993. The effect of block rotations on the global seismic moment tensor and the patterns of seismic P and T axes. Journal of Geophysical Research 98 (B1), 645–674.

Wallace, R.E., 1951. Geometry of shearing stress and relation to faulting. Journal of Geology 59, 118–130.

Xu, P., 2004. Determination of regional stress tensors from fault-slip data. Geophysical Journal International 157, 1316–1330.

Yamaji, A., 2003. Are the solutions of stress inversion correct? Visualization of their reliability and the separation of stress from heterogeneous fault-slip data. Journal of Structural Geology 25, 241–252.

Yin, Z.-M., Ranalli, G., 1993. Determination of tectonic stress field from fault slip data: toward a probabilistic model. Journal of Geophysical Research 98 (B7), 12165–12176.